

Direct coupling of ferromagnetic moment and ferroelectric polarization in BiFeO₃

Shiro Kawachi,¹ Shin Miyahara,² Toshimitsu Ito,³ Atsushi Miyake,⁴
Nobuo Furukawa,⁵ Jun-ichi Yamaura,¹ and Masashi Tokunaga⁴

¹Materials Research Center for Element Strategy,

Tokyo Institute of Technology, Yokohama, Kanagawa 226-8503, Japan.

²Department of Applied Physics, Fukuoka University, Jonan-ku, Fukuoka 814-0180, Japan.

³National Institute of Advanced Industrial Science and Technology (AIST), Tsukuba, Ibaraki 305-8562, Japan.

⁴The Institute for Solid State Physics, The University of Tokyo, Kashiwa, Chiba 277-8581, Japan.

⁵Department of Physics and Mathematics, Aoyama Gakuin University, Sagamihara, Kanagawa 229-8558, Japan.

The spin-driven component of electric polarization in a single crystal of multiferroic BiFeO₃ was experimentally investigated in pulsed high magnetic fields up to 41 T. Sequential measurements of electric polarization for various magnetic field directions provide clear evidence of electric polarization normal to the hexagonal c axis (\mathbf{P}_t) in not only the cycloidal phase, but also the field-induced canted antiferromagnetic phase. The direction of \mathbf{P}_t is directly coupled with the ferromagnetic moment in the canted antiferromagnetic phase, and thus controlled by changing the direction of the applied magnetic field. This magnetoelectric coupling is reasonably reproduced by the metal–ligand hybridization model.

The crossed coupling of magnetism and ferroelectricity in multiferroic materials has unified two major research areas in condensed matter physics that were traditionally distinguished. In addition to being of interest from a point of view of basic science, magnetoelectric coupling is expected to allow the development of innovative devices, such as electrically controllable magnetic memory and multi-bit memory [1, 2]. While most multiferroic materials are active only at low temperatures, BiFeO₃, which exhibits remarkable multiferroic properties at room temperature, has attracted much interest [3].

BiFeO₃ crystallizes in the non-centrosymmetric $R3c$ space group within a trigonal crystal system at temperatures below ~ 1100 K [4]. Atomic displacement from the perovskite-type structure results in spontaneous giant electric polarization \mathbf{P}_s along the hexagonal c axis, which corresponds to $\langle 111 \rangle_c$ in cubic perovskites [the $+Z$ direction in Fig. 1(a)] [3, 5, 6]. The $S = 5/2$ spins of Fe³⁺ ions form a cycloidal magnetic order with the XY -component of the magnetic propagation vector \mathbf{q} pointing in the hexagonal direction $\langle 100 \rangle_h$ below temperatures of ~ 640 K [7]. Three-fold rotational symmetry allows the coexistence of three equivalent magnetic domains [8]. The direction of \mathbf{q} can be controlled by flopping \mathbf{P}_s with an electric field [9, 10]. This flop of \mathbf{P}_s is, however, accompanied by crystal deformation and hence often degrades the crystal, which is unfavorable for application.

In addition to \mathbf{P}_s , BiFeO₃ has parasitic ferroelectric polarization originating from the magnetic order. In the cycloidal phase, BiFeO₃ undergoes a magnetic phase transition with the application of a magnetic field of about 20 T [11]. Extrapolation of the magnetization curve in the field-induced phase to a zero magnetic field has a finite intercept, which suggests the occurrence of the canted antiferromagnetic (CAF) order with a net ferromag-

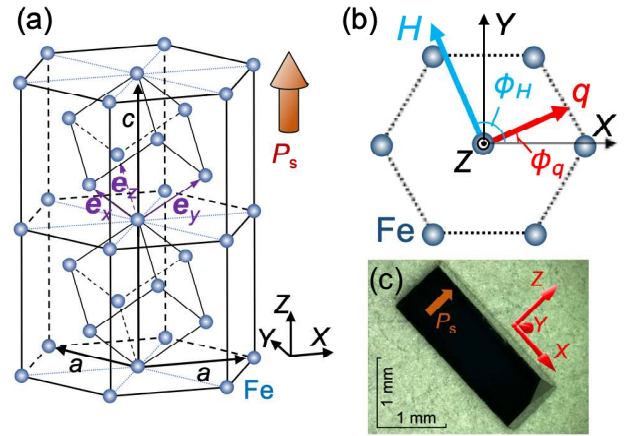


FIG. 1: (a) Illustration of the arrangement of Fe ions in BiFeO₃. \mathbf{a} and \mathbf{c} represent unit vectors in the hexagonal cell. \mathbf{P}_s indicates spontaneous ferroelectric polarization below ~ 1100 K. (b) Schematic drawing of the definition of azimuthal angles for the applied field and cycloidal \mathbf{q} vector, ϕ_H and ϕ_q respectively. (c) Photograph of the single crystal used for the measurements.

netic moment of $\sim 0.04 \mu_B/\text{Fe}$ on the XY plane [11–15]. In general, the cycloidal magnetic order is known to be accompanied by spin-driven electric polarization [16–20]. Field-induced suppression of this phase may affect the electric polarization. Recent experiments using single crystals revealed spin-driven electric polarization in two directions longitudinal and transverse to the Z direction [13, 21–23]. The transverse electric polarization (\mathbf{P}_t) in the cycloidal state is explained by the inverse Dzyaloshinskii–Moriya (DM) model [13, 20, 23], with which the emergence of \mathbf{P}_t normal to the \mathbf{q} - Z plane in a zero field is predicted. Reorientation of magnetic domains is accompanied by the reorientation of \mathbf{P}_t . This

effect appears as a non-volatile memory effect that can be controlled by a magnetic field or electric field even at room temperature [13, 24].

In this study, we determined the direction and absolute value of \mathbf{P}_t and its field-angle dependence in a single crystal of BiFeO₃ through a series of magnetoelectric measurements by changing the direction of the applied magnetic field. The results revealed the doubling of \mathbf{P}_t at the transition from the cycloidal to the CAFM state. Semi-quantitative explanation of the results by the metal–ligand hybridization mechanism clarified the microscopic origin for the spontaneous coupling between ferromagnetism and ferroelectricity in this material, and demonstrated that prominent multiferroic coupling could be realized without complicated spin order.

Single crystals of BiFeO₃ were grown adopting the laser-diode heating floating-zone method [25]. The obtained crystal almost entirely consisted of a single ferroelectric domain of \mathbf{P}_s . A crystal used for the measurements was cut into a rectangular parallelepiped shape of $2.34 \times 0.49 \times 0.85 \text{ mm}^3$ along the crystal axes as shown in Fig. 1(c). To determine the crystal orientation with its chirality, we conducted an x-ray diffraction measurement using a curved imaging plate on a RIGAKU VariMax with RAPID diffractometer at the wavelength of Mo-K α radiation. The crystal chirality was identified by the intensities of Bijvoet-pair-related reflections of $\{6\bar{3}6\}_h$ and $\{6\bar{3}\bar{6}\}_h$ on a hexagonal setting owing to the loss of inversion symmetry based on atomic coordinates given in the literature [4] (See Supplementary Material). The determined a and c hexagonal axes are chosen as the $+X$ and $+Z$ directions. By this definition, \mathbf{P}_s points in the $+Z$ direction as shown in Fig. 1(a). Magnetic-field-induced changes in electric polarization were measured by integrating (de)polarization currents [26] induced in pulsed magnetic fields generated using a 55-T magnet for a duration of 8 ms. These experiments only determined the relative changes in electric polarization (ΔP) with respect to the initial values for a zero field. To determine the zero level of electric polarization, we performed a series of experiments while changing the field angle using a sample rotator as discussed in the following.

Typical results are shown in Fig. 2(a). Prior to this experiment, we applied a magnetic field (H) with a magnitude up to 41 T at an azimuthal angle of $\phi_H = 91^\circ$ ($\sim H \parallel Y$) as defined in Fig. 1(b). We then measured ΔP along the X direction (ΔP_X) as a function of the magnetic field at $\phi_H = 45^\circ$. In the first field cycle, ΔP_X has a hysteretic trace below 10 T [red dotted line in Fig. 2(a)], which is ascribed to the reorientation of the magnetoelectric domains. Here, the change in P_X from 0 to 20 T becomes small after reorientation of the magnetoelectric domain. The generalized inverse DM model predicts the emergence of the largest P_X in the reoriented state

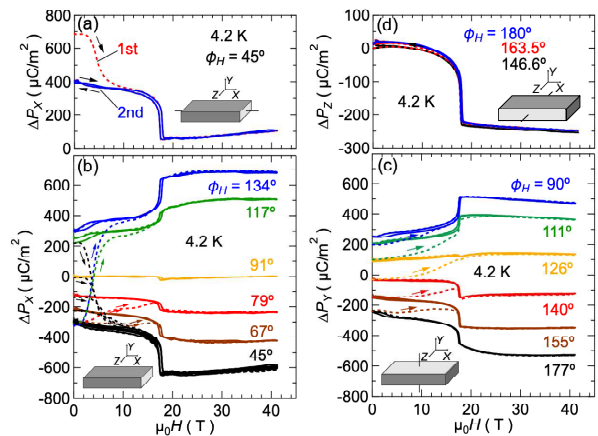


FIG. 2: (a) Magnetic-field-induced changes in electric polarization along X at $\phi_H = 45^\circ$. Traces in the first and second cycles are respectively shown by dotted and solid lines. Magnetic-field-induced changes in electric polarization along (b) X , (c) Y , and (d) Z directions, measured at various field angles. Traces are vertically offset so that the initial point of each curve is the end point of the previous curve. The inset presents a rectangular parallelepiped sample of BiFeO₃ (dark gray area) with electrodes (light gray area) to visualize the measurement direction.

and absence of it in the CAFM state. The observed reduction in ΔP_X is therefore a puzzling phenomenon [13].

To unambiguously determine the spin-driven components in electric polarization, we sequentially measured ΔP_X while systematically changing ϕ_H . Representative data of ΔP_X , ΔP_Y , and ΔP_Z are presented in Figs. 2(b)–(d) as functions of H applied at various ϕ_H . All data presented in the following were recorded at a temperature of 4.2 K to minimize the effect of leakage current. Throughout this letter, P – H curves obtained in the first and second magnetic field sweeps for each ϕ_H are respectively represented by dotted and solid lines. In Figs. 2(b) and 2(c), all traces are offset on the vertical axis so that the starting point of the trace coincides with the endpoint of the previous trace. The curves of ΔP_X in Fig. 2(b) were measured in the order of $\phi_H = 91^\circ \rightarrow 45^\circ \rightarrow 67^\circ \rightarrow 45^\circ \rightarrow 79^\circ \rightarrow 45^\circ \rightarrow 117^\circ \rightarrow 45^\circ \rightarrow 134^\circ$. We here determined the zero level of P_X by taking the average of the largest and smallest values of P_X for a zero field. Adopting the present definition of the zero level, we can reasonably reproduce the observed angular dependence using a theoretical model as will be seen later.

The data at $\phi_H = 134^\circ$ were obtained after application of a field at $\phi_H = 45^\circ$. Thereby, an irreversible change in P_X below 10 T in the first field sweep is due to the 90° rotation of the \mathbf{q} vector, which appears as a sign change in P_X as shown by the blue dotted line. A steep change in P_X at ~ 18 T corresponds to the transition from the cycloidal phase to the CAFM phase. The largest value

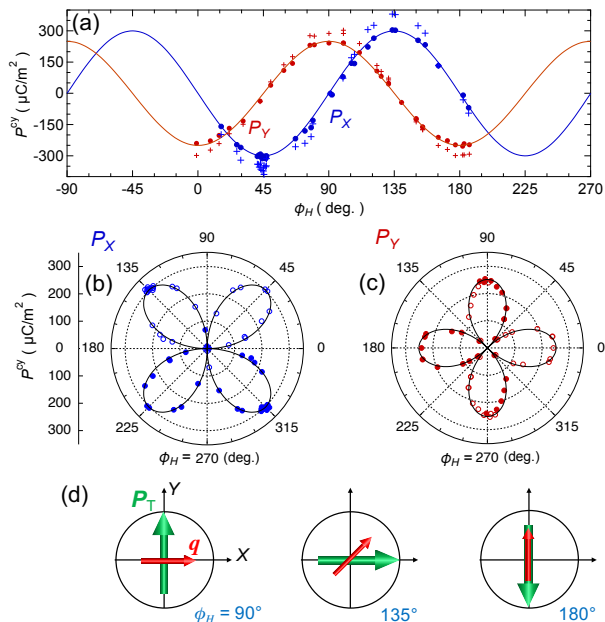


FIG. 3: (a) Angular dependence of the electric polarization along X and Y directions at $\mu_0 H = 0$ and 10 T in the cycloidal phase shown by solid circles and crosses, respectively. The solid line indicates the fitting function of eq. (3) and/or (4) for solid circles at 0 T. Polar plots presenting the dependencies of (b) P_X and (c) P_Y on the magnetic field angle after removal of the magnetic field in the cycloidal phase. Open symbols are projected points of the experimental data at ϕ_H (solid symbols) to $\phi_H + \pi$. (d) Schematics of relative directions between \mathbf{P}_t and the XY component of the \mathbf{q} vector in the cycloidal phase.

of P_X in the cycloidal state is thus determined as $\sim 300 \mu\text{C}/\text{m}^2$ at a zero field. Meanwhile, P_X in the CAFM phase is almost twice this value.

Moreover, we also carried out for P_Y on the same crystal in the order of $\phi_H = 177^\circ \rightarrow 155^\circ \rightarrow 140^\circ \rightarrow 126^\circ \rightarrow 111^\circ \rightarrow 90^\circ$. The results are plotted in Fig. 2(c) adopting a vertical offset as in the previous case. Here, the zero level of P_Y is defined as the average value of P_Y for the zero field after the application of fields along $\phi_H = 90^\circ$ and 177° . We again observe larger P_Y in the CAFM phase for fields stronger than 18 T.

Meanwhile, ΔP_Z has negligible angular dependence as shown in Fig. 2(d). In this case, we can hardly determine the zero level for P_Z . P_Z steeply decreases by $\sim 240 \mu\text{C}/\text{m}^2$; i.e., total P_Z slightly reduces at the cycloid-to-CAFM transition around 18 T independently of the azimuthal angle of the applied field.

Figure 3(a) presents P_X and P_Y as functions of ϕ_H at 0 T in the cycloidal phase (P^{cy}). Here, the data were extracted in the reoriented domain state after the first field cycle at each ϕ_H . According to Bordacs *et al.*, the

direction of the \mathbf{q} vector for a zero field may slightly deviate from the direction perpendicular to the applied field owing to small anisotropy within the XY plane [27, 28]. This deviation, however, plays only a minor role because P_X and P_Y for a field strength of 10 T, which is higher than the strength of pinning threshold fields of ~ 5 T [27], follow almost the same functional forms as shown by crosses in Fig. 3(a). Figures 3(b) and 3(c) exhibit polar plots of the P_X and P_Y shown in Fig. 3(a). The solid circles represent the experimental data, while the open ones are projection of the data at ϕ_H to $\phi_H + \pi$. For some field angles, we confirmed that the magnetoelectric effect appears symmetric with respect to the sign change in the applied field as shown in Supplementary Material.

Continuous changes in P_X and P_Y indicate that ϕ_q smoothly follows changes in ϕ_H in the cycloidal state. As for the slight difference between the amplitudes of P_X and P_Y , we cannot rule out possible error in the estimation of the effective surface area of the sample. P_X and P_Y respectively trace simple functions of $-P_t \sin 2\phi_H$ and $-P_t \cos 2\phi_H$. This means that \mathbf{P}_t rotates in the XY plane while the magnitude is almost unchanged.

Figure 3(d) illustrates the relationship between \mathbf{P}_t and \mathbf{q} on the XY plane determined by the experimental data at several magnetic field angles in the cycloidal phase; $\mathbf{q} \perp \mathbf{P}_t$ at $\phi_H = (1/2 + 2n/3)\pi$ and $\mathbf{q} \parallel \mathbf{P}_t$ at $\phi_H = 2\pi n/3$ with integer n . \mathbf{P}_t rotates in the opposite direction to the magnetic field.

Figures 4(a)–4(c) show the ϕ_H dependencies of P_X and P_Y at 40 T in the CAFM phase. P_X and P_Y have the same functional formula as in the cycloidal phase. The relative orientation determined experimentally between the ferromagnetic component in the CAFM state (\mathbf{m}) and \mathbf{P}_t is schematically shown in Fig. 4(d). \mathbf{m} follows a curve parallel to \mathbf{H} owing to the Zeeman energy [13, 14], while \mathbf{P}_t rotates in the opposite direction to the rotation of \mathbf{H} by a double angle. This result means that if we rotate \mathbf{m} at a frequency of ω , we will have rotation of \mathbf{P}_t at the frequency of 2ω .

Let us discuss the origin for \mathbf{P}_t coupled with the magnetic order. The multiferroic behavior is usually reproduced using spin-dependent electric polarization:

$$p_i^\alpha = \sum_{\beta\gamma} \Lambda_{\beta\gamma}^\alpha S_i^\beta S_i^\gamma \quad (1)$$

$$p_{ij}^\alpha = \Pi_{ij}^\alpha \mathbf{S}_i \cdot \mathbf{S}_j + \sum_{\beta} d_{ij}^{\alpha\beta} (\mathbf{S}_i \times \mathbf{S}_j)^\beta, \quad (2)$$

where $\alpha, \beta, \gamma = X, Y, Z$ and $\Lambda, \Pi_{ij}, d_{ij}$ are coupling constants [29]. p_i is a single-spin term that is induced by metal–ligand hybridization (ML) and p_{ij} is a spin pair term that includes the electric polarization induced by symmetric exchange striction (ES) and antisymmetric inverse DM interaction. We consider \mathbf{p}_i at Fe ion sites and

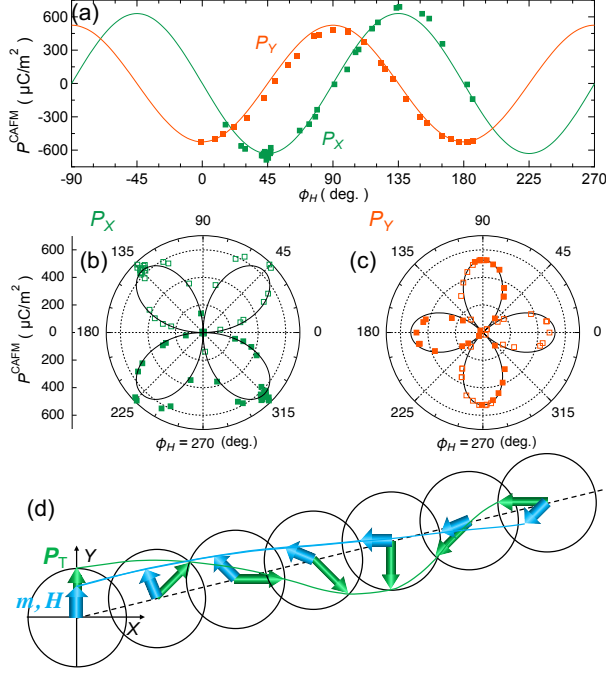


FIG. 4: (a) Field-angle dependence of the electric polarization along X (orange) and Y (green) directions at $\mu_0 H = 40$ T in the CAFM phase. The solid line shows the fitting functions of P_X and P_Y obtained using eq. (3). Polar plots represent the magnetic-field-angle dependencies of (b) P_X and (c) P_Y at 40 T in the CAFM phase. Experimental data and a theoretical curve are respectively shown by symbols and a solid line. The open symbols are a projection of experimental data at ϕ_H (solid symbols) to $\phi_H + \pi$. (d) Schematic relation between the ferromagnetic moment (blue arrow) and \mathbf{P}_t (green arrow) in the CAFM phase.

\mathbf{p}_{ij} for the nearest neighboring pair of Fe ions. Locations of Fe ions are represented by $\mathbf{r}_i = n_i^x \mathbf{e}_x + n_i^y \mathbf{e}_y + n_i^z \mathbf{e}_z$ for a set of integers (n_i^x, n_i^y, n_i^z) and unit vectors $\mathbf{e}_x, \mathbf{e}_y$, and \mathbf{e}_z connecting adjacent Fe sites as shown in Fig. 1(a). The non-zero terms of \mathbf{p}_i in BiFeO₃ are originated from a C_3 point group [30] and any term of \mathbf{p}_{ij}^α is allowed to be non-zero from a symmetry argument [20]. We defined the coupling constants of \mathbf{p}_{ij}^α for one of the bonds along \mathbf{e}_z as eqs. (S2) and (S3) in the Supplementary Material; (e.g., $\Pi^X \equiv \Pi_{ii+z}^X$, $d^{XY} \equiv d_{ii+z}^{XY}$), and the other coupling constants for the inequivalent five bonds are expressed using the rotational-symmetry operation.

The spin at the i -th site can be represented as $\mathbf{S}_i = (S \cos \phi_q \sin \mathbf{q} \cdot \mathbf{r}_i, S \sin \phi_q \sin \mathbf{q} \cdot \mathbf{r}_i, S \cos \mathbf{q} \cdot \mathbf{r}_i)$ and $\mathbf{S}_i = \{S \sin [\eta + (-1)^{n_i} \phi_H], -(-1)^{n_i} S \cos [\eta + (-1)^{n_i} \phi_H], 0\}$ in cycloidal and CAFM states, respectively, whereas $\mathbf{q} = (q_0 \cos \phi_q, q_0 \sin \phi_q, \sqrt{3}\pi/a_c)$ and $q_0 = 2\pi/\lambda$ with the cycloidal period $\lambda = 620$ Å and lattice constant of the pseudocubic cell $a_c = 3.96$ Å. η ($\ll 1$) represents the spin canting angle in the CAFM state. In the cycloidal state, we ignore the minor spin component normal to

TABLE I: Values of P_t^0 in the eq. (3) of IDM, ES, and ML mechanisms in the cycloidal and CAFM phases, respectively. Details of these calculations are described in Supplementary Material.

	IDM	EX	ML
Cycloid	$\frac{\sqrt{6}}{4} q_0 a_c S^2 (d^{XY} + d^{YX})$	$\frac{(q_0 a_c)^2}{2} S^2 \Pi_Y$	$-\frac{1}{2} S^2 \Lambda_{XY}^X$
CAFM	0	0	$-S^2 \Lambda_{XY}^X$

the \mathbf{q} - \mathbf{Z} plane [31] for simplicity.

By taking the spatial average in the cycloidal state, we can evaluate macroscopic polarizations as described in Supplementary Material. In the cycloidal state, all mechanisms expressed in eqs. (1) and (2) can explain the emergence of spin-driven electric polarization \mathbf{P}_{mag} in the form

$$\mathbf{P}_{\text{mag}} = (-P_t^0 \sin 2\phi_H, -P_t^0 \cos 2\phi_H, P_Z). \quad (3)$$

Here, P_t^0 in each phase is tabulated in Table I. As shown by the solid lines in Figs. 3(a)–3(c), eq. (3) reasonably reproduces the experimental results for the cycloidal state when setting $\phi_H = \phi_q + \pi/2$ and $P_t^0 \sim 300 \mu\text{C}/\text{m}^2$. In the CAFM phase, ϕ_H dependence is again expressed by eq. (3). Here, ES and IDM mechanisms suggest $P_t^0 = 0$ contrary to the experimental results. On the other hand, the ML mechanism predicts doubling of the P_t^0 in the CAFM phase. This predicted doubling of P_t^0 together with the characteristic angular dependence in eq. (3) reasonably reproduce the experimental results as shown in Figs. 4(b) and 4(c). Therefore, spin-induced polarization in the cycloidal and CAFM phases can mainly be ascribed to the ML mechanism.

In the ML mechanism, spin-driven electric polarization is determined by the local spin component at each Fe ion. For example, amplitude of p_i^Y is proportional to $(S_i^X)^2$ when $\phi_H = \pi/2$ ($\phi_q = 0$) as shown in Supplementary Material. In the cycloidal state, spatial average of sinusoidally changing $(S_i^X)^2$, namely sinusoidally modulating p_i^Y , results in the reduction of P_Y by a factor of 1/2 from that in the CAFM state.

Finite magnetoelectric effects in the CAFM phase have been argued in some earlier reports [11, 14, 32, 33]. Different from the earlier arguments, our results indicate emergence of the spontaneous electric polarization in the CAFM phase even in the zero-field limit, which is crucially important to utilize the CAFM states in thin films or Co-substituted BiFeO₃ at zero field [34, 35]. Although we studied the magnetic control of \mathbf{P}_t in the CAFM phase at a temperature of 4.2 K, this phase exists up to a temperature higher than room temperature [36]. In addition, the P_t^0 remains finite in the limit of $\eta \rightarrow 0$ meaning simple collinear antiferromagnetic state can induce spin-driven polarization in this material. In many multiferroic materials, frustrated spin systems have been widely

studied to realize complicated spin structures, which results in low ordering temperature. The present result suggests that magnetically controllable electric polarization of $\sim 600 \mu\text{C}/\text{m}^2$ can be realized even in a simple antiferromagnet. This finding will pave a way to develop multiferroic materials useful at room temperature.

In summary, we measured the angular dependence of field-induced changes in the electric polarization for a single crystal of BiFeO_3 . The electric polarization normal to the hexagonal axis was systematically controlled by changing the azimuthal angle of the applied magnetic field. Results reveal that this component is strengthened by the field-induced transition from the cycloidal phase to the canted antiferromagnetic phase. We explained this spin-driven component of electric polarization using the metal–ligand hybridization mechanism.

This work was supported by the JSPS Grant No. JP16K05413 and the MEXT Element Strategy Initiative to Form Core Research Center.

-
- [1] M. Bibes and A. Barthélemy, *Nat. Mater.* **7**, 425 (2008).
 [2] J. F. Scott, *Nat. Mater.* **6**, 256 (2007).
 [3] G. Catalan and J. F. Scott, *Adv. Mater.* **21**, 2463 (2009).
 [4] B. F. Kubel and H. Schmid, *Acta Cryst. B* **46**, 698 (1990).
 [5] V. V. Shvartsman, W. Kleemann, R. Haumont, and J. Kreisel, *Appl. Phys. Lett.* **90**, 172115 (2007).
 [6] D. Lebeugle, D. Colson, A. Forget, M. Viret, P. Bonville, J. F. Marucco, and S. Fusil, *Phys. Rev. B* **76**, 024116 (2007).
 [7] I. Sosnowska, T. Peterlin-Neumaier, and E. Steichele, *J. Phys. C* **15**, 4835 (1982).
 [8] R. D. Johnson, P. Barone, A. Bombardi, R. J. Bean, S. Picozzi, P. G. Radaelli, Y. S. Oh, S.-W. Cheong, and L. C. Chapon, *Phys. Rev. Lett.* **110**, 217206 (2013).
 [9] D. Lebeugle, D. Colson, A. Forget, M. Viret, A. M. Bataille, and A. Gukasov, *Phys. Rev. Lett.* **100**, 227602 (2008).
 [10] S. Lee, T. Choi, W. Ratcliff II, R. Erwin, S.-W. Cheong, and V. Kiryukhin, *Phys. Rev. B* **78**, 100101(R) (2008).
 [11] A. Kadomtseva, A. Zvezdin, Y. Popov, A. Pyatakov, and G. Vorobev, *JETP Lett.* **79**, 571 (2004).
 [12] B. Ruetter, S. Zvyagin, A. P. Pyatakov, A. Bush, J. F. Li, V. I. Belotelov, A. K. Zvezdin, and D. Viehland, *Phys. Rev. B* **69**, 064114 (2004).
 [13] M. Tokunaga, M. Akaki, T. Ito, S. Miyahara, A. Miyake, H. Kuwahara, and N. Furukawa, *Nat. Commun.* **6**, 5878 (2015).
 [14] S. Kawachi, A. Miyake, T. Ito, S. E. Dissanayake, M. Matsuda, W. Ratcliff II, Z. Xu, Y. Zhao, S. Miyahara, N. Furukawa, and M. Tokunaga, *Phys. Rev. Materials* **1**, 024408 (2017).
 [15] A. P. Pyatakov and A. K. Zvezdin, *Eur. Phys. J. B* **71**, 419 (2009).
 [16] H. Katsura, N. Nagaosa, and A. V. Balatsky, *Phys. Rev. Lett.* **95**, 057205 (2005).
 [17] T. Arima, *J. Phys. Soc. Jpn.* **80**, 052001 (2011).
 [18] T. A. Kaplan and S. D. Mahanti, *Phys. Rev. B* **83**, 174432 (2011).
 [19] A. P. Pyatakov, A. S. Sergeev, F. A. Mikailzade, and A. K. Zvezdin, *J. Magn. Magn. Mater.* **383**, 255 (2015).
 [20] S. Miyahara and N. Furukawa, *Phys. Rev. B* **93**, 014445 (2016).
 [21] J. Park, S.-H. Lee, S. Lee, F. Gozzo, H. Kimura, Y. Noda, Y. J. Choi, V. Kiryukhin, S.-W. Cheong, Y. Jo, E. S. Choi, L. Balicas, G. S. Jeon, and J.-G. Park, *J. Phys. Soc. Jpn.* **80**, 114714 (2011).
 [22] S. Lee, M. T. Fernandez-Diaz, H. Kimura, Y. Noda, D. T. Adroja, S. Lee, J. Park, V. Kiryukhin, S.-W. Cheong, M. Mostovoy, and J.-G. Park, *Phys. Rev. B* **88**, 060103(R) (2013).
 [23] J. H. Lee and R. S. Fishman, *Phys. Rev. Lett.* **115**, 207203 (2015).
 [24] S. Kawachi, H. Kuroe, T. Ito, A. Miyake, and M. Tokunaga, *Appl. Phys. Lett.* **108**, 162903 (2016); **110**, 239902 (2017).
 [25] T. Ito, T. Ushiyama, Y. Yanagisawa, R. Kumai, and Y. Tomioka, *Cryst. Growth Des.* **11**, 5139 (2011).
 [26] H. Mitamura, S. Mitsuda, S. Kanetsuki, H. A. Katori, T. Sakakibara, and K. Kindo, *J. Phys. Soc. Jpn.* **76**, 094709 (2007).
 [27] S. Bordács, D. G. Farkas, J. S. White, R. Cubitt, L. DeBeer-Schmitt, T. Ito, and I. Kézsmárki, *Phys. Rev. Lett.* **120**, 147203 (2018).
 [28] R. S. Fishman, *Phys. Rev. B* **97**, 014405 (2018).
 [29] T. Moriya, *J. Appl. Phys.* **39**, 1042 (1968).
 [30] M. Matsumoto, K. Chimata and M. Koga, *J. Phys. Soc. Jpn.* **86**, 034704 (2017).
 [31] M. Ramazanoglu, M. Laver, W. Ratcliff II, S. M. Watson, W. C. Chen, A. Jackson, K. Kothapalli, S. Lee, S. -W. Cheong, and V. Kiryukhin, *Phys. Rev. Lett.* **107**, 207206 (2011).
 [32] Y. F. Popov, A. M. Kadomtseva, S. S. Krotov, D. V. Belov, G. P. Vorob'ev, P. N. Makhov, and A. K. Zvezdin, *Low Temp. Phys.* **27**, 478 (2001).
 [33] M. Tokunaga, M. Akaki, A. Miyake, T. Ito, and H. Kuwahara, *J. Mag. Mag. Mater.* **383**, 259 (2015).
 [34] H. Yamamoto, T. Kihara, K. Oka, M. Tokunaga, K. Mibu, and M. Azuma, *J. Phys. Soc. Jpn.* **85**, 064704 (2016).
 [35] D. Sando, A. Agbelele, D. Rahmedov, J. Liu, P. Rovillain, C. Toulouse, I. C. Infante, A. P. Pyatakov, S. Fusil, E. Jacquet, C. Carretero, C. Deranlot, S. Lisenkov, D. Wang, J.-M. Le Breton, M. Cazayous, A. Sacuto, J. Juraszek, A. K. Zvezdin, L. Bellaïche, B. Dkhil, A. Barthelemy, and M. Bibes, *Nat. Mater.* **12**, 641 (2013).
 [36] M. Tokunaga, M. Azuma, and Y. Shimakawa, *J. Phys. Soc. Jpn.* **79**, 064713 (2010).